

IMPACT OF CLUSTER PHYSICS ON THE SUNYAEV-ZEL'DOVICH POWER SPECTRUM

LAURIE D. SHAW^{1,2}, DAISUKE NAGAI^{1,2}, SUMAN BHATTACHARYA³, ERWIN T. LAU⁴

Draft version October 25, 2018

ABSTRACT

We use an analytic model to investigate the theoretical uncertainty on the thermal Sunyaev-Zel'dovich (SZ) power spectrum due to astrophysical uncertainties in the thermal structure of the intracluster medium. Our model accounts for star formation and energy feedback (from supernovae and active galactic nuclei) as well as radially dependent non-thermal pressure support due to random gas motions, the latter calibrated by recent hydrodynamical simulations. We compare the model against X-ray observations of low redshift clusters, finding excellent agreement with observed pressure profiles. Varying the levels of feedback and non-thermal pressure support can significantly change both the amplitude and shape of the thermal SZ power spectrum. Increasing the feedback suppresses power at small angular scales, shifting the peak of the power spectrum to lower ℓ . On the other hand, increasing the non-thermal pressure support has the opposite effect, significantly reducing power at large angular scales. In general, including non-thermal pressure at the level measured in simulations has a large effect on the power spectrum, reducing the amplitude by 50% at angular scales of a few arcminutes compared to a model without a non-thermal component. Our results demonstrate that measurements of the shape of the power spectrum can reveal useful information on important physical processes in groups and clusters, especially at high-redshift where there exists little observational data. Comparing with the recent South Pole Telescope measurements of the small-scale cosmic microwave background power spectrum, we find our model reduces the tension between the values of σ_8 measured from the SZ power spectrum and from cluster abundances.

Subject headings: cosmology: dark matter — galaxies: clusters: general — intergalactic medium

1. INTRODUCTION

The Sunyaev-Zel'dovich (SZ) effect has long been recognized as a powerful tool for probing the physics of the intracluster medium (ICM), large-scale structure formation and the dark energy equation of state (Birkinshaw 1999; Carlstrom et al. 2002). Experiments such as the South Pole Telescope (Ruhl et al. 2004), the Atacama Cosmology Telescope (Kosowsky 2003) and Planck⁵ are currently surveying the microwave sky with the goal of identifying clusters via their SZ signature on the cosmic microwave background (CMB), thus constructing large catalogs of galaxy clusters that are uniformly selected by SZ flux (Vanderlinde et al. 2010).

The SZ effect can also be detected as a secondary anisotropy in the CMB temperature power spectrum, appearing as “excess power” (over the predicted primary anisotropy signal) on angular scales of a few arcminutes. The ensemble averaged power spectrum amplitude \bar{C}_ℓ has an extremely sensitive dependence on σ_8 , $\bar{C}_\ell \propto \sigma_8^7 (\Omega_b h)^2$ (Komatsu & Seljak 2002), where σ_8 is the power spectrum normalization on scales of $8h^{-1}$ Mpc. The SZ angular power spectrum thus represents a robust observable with which competitive constraints on σ_8 can be obtained. This would in turn enable tighter

constraints to be placed on the dark energy equation of state parameter w by breaking the degeneracy with σ_8 in constraints derived from the primary CMB signal alone.

A number of experiments have reported detections of power in excess of the primary CMB power spectrum at small angular scales and thus been able to place upper limits on the amplitude of the SZ signal (Dawson et al. 2006; Friedman & QUaD Collaboration 2009; Reichardt et al. 2009a,b; Sievers et al. 2009; Sharp et al. 2010; Fowler et al. 2010). The South Pole Telescope (SPT, Lueker et al. 2010) has recently reported measurements of the CMB power spectrum at 150 GHz for angular scales in the range $2000 < \ell < 10000$. By combining SPT survey maps at 150 and 220 GHz to minimize astrophysical foreground signals, Lueker et al. (2010) were able to isolate and detect SZ power (kinetic plus thermal) at 2.6σ . The measured amplitude at $\ell = 3000$ was $4.2 \pm 1.5 \mu K^2$, significantly below that predicted by halo model calculations (Komatsu & Seljak 2002) or simulations (White et al. 2002; Shaw et al. 2009; Sehgal et al. 2010), assuming WMAP7 cosmological parameters. The significantly lower-than-predicted signal could be explained by a lower value of σ_8 . Using the SZ power spectrum predicted by simulations and assuming no modeling uncertainty, Lueker et al. (2010) measured $\sigma_8 = 0.746 \pm 0.017$. However, this result is in tension with other probes of σ_8 ; for example, recent X-ray and optical measurements of cluster abundances suggest $\sigma_8 = 0.82 \pm 0.05$ (Mantz et al. 2010), $\sigma_8 (\Omega_M/0.25)^{0.47} = 0.813 \pm 0.013$ (Vikhlinin et al. 2009), and $\sigma_8 = 0.807 \pm 0.02$ (Roza et al. 2010).

This disagreement can be resolved if current analytic models and simulations over-predict the level of SZ power

¹ Department of Physics, Yale University, New Haven, CT 06520

² Yale Center for Astronomy & Astrophysics, Yale University, New Haven, CT 06520

³ T-2, Theoretical Division, Los Alamos National Laboratory, Los Alamos, NM 87545

⁴ Department of Astronomy & Astrophysics, 5640 South Ellis Ave., The University of Chicago, Chicago, IL 60637
laurie.shaw@yale.edu

⁵ <http://www.rssd.esa.int/index.php?project=Planck>

by a factor of ≈ 2 . SZ power spectrum calculations have two sources of uncertainties: the amplitude of the halo mass function, and in modeling the radial electron pressure profile of the ICM. Recent studies of the mass and redshift distribution of halos in N-body simulations imply that the mass function is known to 5%-10% accuracy for the currently allowed Λ CDM cosmology (Tinker et al. 2008; Bhattacharya et al. 2010a) and so is not the dominant theoretical uncertainty (although, as pointed out by Stanek et al. 2009, the impact of baryonic physics on halo masses is still somewhat unclear).

The main difficulty in calculating the thermal SZ (tSZ) power spectrum is predicting the thermal pressure profiles of groups and clusters over a wide range of mass and redshift. Komatsu & Seljak (2002) and Holder (2002) show that low-mass ($M < 2 \times 10^{14} h^{-1} M_\odot$) and high-redshift ($z > 0.6$) objects both make a significant contribution to the signal at angular scales of a few arcminutes ($\ell \approx 4000$), the scales at which current small-scale anisotropy experiments such as SPT are most sensitive. While *Chandra* and *XMM-Newton* have enabled high-mass, low-redshift clusters to be studied extensively over the last decade, lower mass and, in particular, high-redshift objects have not been extensively studied. Furthermore, the SZ power spectrum is sensitive to the thermal pressure of the ICM out to cluster radii several times larger than is typically probed by X-ray observations. Hence, there are few observational constraints that can be used to aid predictions of the tSZ power spectrum.

From a theoretical perspective, full cosmological hydrodynamical simulations have only recently begun to systematically explore the effects of sub-grid baryonic processes, such as radiative cooling, star formation, feedback mechanisms, cosmic rays, thermal conduction and magnetic fields, on the thermal structure of the ICM (Nagai et al. 2007a; Pfrommer et al. 2007; Dolag & Stasyszyn 2009; Sijacki et al. 2007, 2008; Battaglia et al. 2010). Furthermore, simulations require high spatial resolution in order to effectively implement some of these processes. However, large box sizes are also required in order to adequately sample the halo mass function at group and cluster scales to enable measurements of the tSZ power spectrum. Currently, the computational expense of running large box, high-resolution hydrodynamical simulations is prohibitive to investigating the level of theoretical uncertainty on the power spectrum as well as the dependence on cosmological parameters.

The principal aim of this work is to use analytic models to investigate variations in the predicted tSZ power spectrum caused by uncertainties in the thermal structure of the ICM. Specifically, we study the impact of energy feedback, non-thermal pressure support and halo concentration on the shape and amplitude of the power spectrum. This is achieved by combining an analytic model for the ICM with the halo mass function to rapidly calculate the power spectrum for different model parameters. Our model assumes that gas resides in hydrostatic equilibrium with a polytropic equation of state, and accounts for star-formation as well as feedback from supernovae and active galactic nuclei (AGNs) and non-thermal pressure support driven by random gas motions and turbulence in the ICM. We calibrate our model parameters by comparing against X-ray observations of mas-

sive, low- z clusters. We find that including non-thermal pressure support at the level measured in state-of-the-art hydrodynamical simulations significantly reduces the amplitude of the predicted tSZ power spectrum, thus reducing the tension between the σ_8 inferred from the SPT observations and cluster abundance measurements.

The paper is organized as follows. In Section 2, we describe our model of the ICM. In Section 3, we explore the model parameter space by comparing model scaling relations and radial profiles against recent low-redshift X-ray observations of groups and clusters. In Section 4, we explore the uncertainty on the tSZ power spectrum sourced by the underlying range in ICM model parameters. We compare our fiducial power spectrum model with other recent simulations, and discuss our results in the context of the recent SPT observations.

Throughout this paper we assume a fiducial, spatially flat, Λ CDM cosmological model consistent with the WMAP7 best-fit cosmological parameters, namely $H_0 = 71 \text{ km s}^{-1} \text{ Mpc}^{-1}$, $\Omega_M = 0.264$, $\Omega_b = 0.044$, $\Omega_\Lambda = 0.736$, $n_s = 0.96$ and $\sigma_8 = 0.8$.

2. THEORETICAL MODELS

2.1. Thermal SZ Power Spectrum

The tSZ effect is a distortion of the CMB caused by inverse Compton scattering of CMB photons off electrons in the high temperature plasma within galaxy clusters. To first order, the temperature change at frequency ν of the CMB is given by $\Delta T/T_{\text{CMB}}(x_\nu) = f(x_\nu)y$, where $f(x_\nu) = x_\nu(\coth(x_\nu/2) - 4)$, $x_\nu = h\nu/k_B T_{\text{CMB}}$, and y is the dimensionless Compton- y parameter

$$y = \left(\frac{k_B \sigma_T}{m_e c^2} \right) \int n_e(l) T_e(l) dl, \quad (1)$$

where the integral is along the line of sight, T_{CMB} is the CMB temperature, and n_e and T_e are the number density and electron temperature of the ICM, respectively.

The tSZ power spectrum can be calculated by simply summing up the squared Fourier-space SZ profiles of all clusters:

$$C_\ell = f(x_\nu)^2 \int dz \frac{dV}{dz} \int d \ln M \frac{dn(M, z)}{d \ln M} \tilde{y}^2(M, z, \ell) \quad (2)$$

where $V(z)$ is the comoving volume per steradian and $n(M, z)$ is the number density of objects of mass M at redshift z . For the latter we use the fitting function of Tinker et al. (2008). $\tilde{y}(M, z, \ell)$ is the Fourier transform of the projected SZ profile for a cluster of mass M and redshift z . This can be calculated assuming spherical symmetry using (Bracewell 2000; Komatsu & Seljak 2002):

$$\tilde{y}(M, z, \ell) = \frac{4\pi r_c}{\ell_c^2} \int_0^\infty dx x^2 P_y(M, z, x) \frac{\sin(\ell x/\ell_c)}{\ell x/\ell_c}, \quad (3)$$

where $x = r/r_c$, $\ell_c = D_A(z)/r_c$, r_c is a characteristic scale radius of the profile, $D_A(z)$ is the angular diameter distance to redshift z and $p_y(M, z, x)$ is the three-dimensional SZ profile, which is related simply to the gas thermal electron pressure profile,

$$P_y(M, z, x) \equiv \frac{\sigma_T}{m_e c^2} P_e(M, z, x). \quad (4)$$

Note that while this calculation only accounts for the

one-halo contribution to C_ℓ , Komatsu & Kitayama (1999) demonstrated that, at the angular scales being probed by the current generation of small-scale CMB experiments (i.e., $\ell \geq 1000$), the two-halo (or clustered) contribution to the tSZ power spectrum is nearly 2 orders of magnitude smaller than the one-halo term and decreases with increasing ℓ . We thus neglect the two-halo contribution in our calculation.

Groups and clusters over a wide mass ($10^{13} < M/M_\odot < 10^{15}$) and redshift ($0 < z < 3$) range contribute to the tSZ power spectrum. For example, more than half the power at $\ell = 3000$ comes from clusters at redshift greater than one (Komatsu & Seljak 2002). Likewise, at the same angular scale, half of the power is predicted to be sourced by objects of mass less than $2 \times 10^{14} M_\odot$. While the mass and redshift contribution depends on the details of the underlying gas physics incorporated in models and simulations, it is clear that much of the signal comes from objects for which there exists little direct observational data.

2.2. Cluster Model

Our model for the density and temperature structure of the ICM is based upon the model of Ostriker et al. (2005, henceforth O05) and Bode et al. (2009, henceforth B09), with an important modification that allows for a radially-dependent non-thermal pressure component (e.g., turbulence or bulk flows). In this section, we briefly review the model and describe how non-thermal pressure support is implemented; we refer the reader to O05 and B09 for a more detailed description of the original model.

2.2.1. Dark Matter Halo Structure

The model assumes that the ICM initially follows the density and temperature of the host dark matter halo, but rapidly rearranges into hydrostatic equilibrium within the potential well of the host dark matter halo with a polytropic equation of state.

Dark matter halo properties are determined by a Navarro-Frenk-White (NFW) density profile (Navarro et al. 1996, 1997) of the form,

$$\rho_{DM}(r) = \frac{\rho_s}{x(1+x)^2}, \quad (5)$$

where $x \equiv r/r_s$, r_s is the NFW scale radius, and ρ_s is a normalization constant. Halo concentration is defined as $c \equiv R_{\text{vir}}/r_s$. Numerous N-body simulations have demonstrated there to be a power-law scaling between halo mass, redshift and concentration. We adopt the halo mass-concentration relation measured by Duffy et al. (2008) from halos identified in a large N-body simulation over the redshift range $0 \leq z \leq 2$,

$$c(M, z) = 7.85 A_C \left(\frac{M_{\text{vir}}}{2 \times 10^{12} h^{-1} M_\odot} \right)^{-0.081} (1+z)^{-0.71}, \quad (6)$$

where A_C is an arbitrary normalization factor that we will later vary to investigate the impact of the mass-concentration normalization on the tSZ power spectrum through our model. $A_C = 1$ gives the mass-concentration relation of Duffy et al. (2008).

Halo masses are defined in terms of the virial overden-

sity;

$$M_{\text{vir}} = \frac{4}{3} R_{\text{vir}}^3 \Delta_c \rho_c(z), \quad (7)$$

where $\Delta_c = 18\pi^2 + 82(\Omega_M(z) - 1) - 39(\Omega_M(z) - 1)^2$ is the virial overdensity given in Bryan & Norman (1998) and $\rho_c(z)$ is the critical density at redshift z . When comparing with observations, we also use the mass definition $M_{500} = (4/3)\pi R_{500}^3 500\rho_c$, where R_{500} is the radius out to which current X-ray observations can reliably measure the gas density and temperature profiles.

2.2.2. Star Formation

The gas is initially treated as a tracer of negligible mass of the dark matter gravitational potential, i.e., it does not contribute itself to the gravitational potential of the cluster and the gas density and temperature follows that of the dark matter.

We assume that some fraction of the gas has radiatively cooled and formed stars. To determine the stellar mass of a cluster we use the observed scaling relation of Giodini et al. (2009), who measured the ratio of stellar mass to total mass for 91 X-ray selected groups and low-mass clusters in the COSMOS survey (Scoville et al. 2007). This was supplemented by the 27 low-redshift, X-ray selected clusters analyzed by (Lin et al. 2003), resulting in an overall sample that encompassed a wide range of both mass ($10^{13} \leq M_{500} \leq 10^{15}$) and redshift ($0 \leq z \leq 1$). They found that the stellar mass fraction within R_{500} , $f_*(< R_{500}) = M_*(< R_{500})/M_{500}$, followed a mean empirical relation;

$$f_* = (2.58 \pm 0.05) \times 10^{-2} \left(\frac{M_{500}}{3 \times 10^{14} M_\odot} \right)^{-0.37 \pm 0.04}. \quad (8)$$

We assume that the stellar mass fraction given above also holds within R_{vir} , i.e., $f_* = M_*(< R_{500})/M_{500} = M_*(< R_{\text{vir}})/M_{\text{vir}}$. Following O05 and B09, we determine the redshift evolution of the stellar mass fraction adopting the ‘‘fossil’’ model of Nagamine et al. (2006). In this model the star-formation rate is given by a delayed exponential, with a decay time of 1.5 Gyr for bulge populations and 4.5 Gyr for disk populations. This model predicts only a small ($\approx 15\%$) decrease between $z = 0$ and 1 in the normalization of this relation, which is consistent with the results of Giodini et al. (2009).

The initial total gas mass within the virial radius is thus

$$M_{g,i} = (f_b - f_*) M_{\text{vir}} \quad (9)$$

and the initial total energy of the gas is

$$E_{g,i} = f_b \left[2\pi \int_{r_*}^{R_{\text{vir}}} \rho_{DM}(r) 3\sigma_{DM}^2(r) r^2 dr + \int_{r_*}^{R_{\text{vir}}} \Phi(r) \frac{dM}{dr} dr \right], \quad (10)$$

where $f_b = \Omega_b/\Omega_M$, $\Phi(r)$ is the gravitational potential and $\sigma_{DM}(r)$ is the one-dimensional dark matter velocity dispersion (see, for example, Equation (13) of Lokas & Mamon 2001, and we assume isotropic dark matter orbits). Thus, the initial total energy of the gas is simply the sum of the kinetic and potential energy of the dark matter halo scaled by the cosmic baryon fraction. We assume that the gas within a radius r_* has cooled and formed stars, where r_* is determined by

$f_b M_{DM}(< r_*) = f_* M_{vir}$ and so omit the contribution to the total gas energy within this radius ($r_* \approx 0.24$ Mpc for a $2 \times 10^{14} h^{-1} M_\odot$ cluster at $z = 0.5$, decreasing weakly toward higher redshift/lower mass). We note that the final gas mass within R_{vir} predicted by our model is not necessarily equal to $M_{g,i}$, as the gas may expand or contract when hydrostatic equilibrium is enforced (see Section 2.2.4).

2.2.3. Hydrostatic Equilibrium

The ICM should rapidly rearrange itself into hydrostatic equilibrium, satisfying

$$\frac{dP_{tot}(r)}{dr} = -\rho_g(r) \frac{d\Phi(r)}{dr}, \quad (11)$$

where $\rho_g(r)$ is the gas density at radius r from the cluster center and P_{tot} is the total gas pressure, $P_{tot}(r) = P_{th}(r) + P_{nt}(r)$. The total gas pressure is therefore a combination of the thermal and non-thermal pressure components, with the latter primarily due to random gas motions and turbulence in the ICM. We discuss how we implement a non-thermal pressure component in the following section.

Hydrodynamical simulations indicate that the *total* pressure adheres more closely to a polytropic equation of state than the thermal pressure, i.e., $P_{tot} \propto \rho_g^\Gamma$. Figure 1 shows the pressure-density phase diagram obtained for 16 clusters simulated using the Eulerian hydrodynamics ART code (Kravtsov et al. 2002), including radiative cooling and star formation (Nagai et al. 2007a). The total pressure (blue line) is the sum of the thermal (red line) and non-thermal components in radial bins around the cluster potential minimum, averaged over the entire sample. The shaded regions denote the standard deviation within the sample around the mean. The non-thermal pressure is measured from the radial velocity dispersion of the gas within each shell (Lau et al. 2009). The black dashed line represents $\Gamma = 1.2$.

It is clear from this figure that using the total pressure results in a constant adiabatic index of 1.2 over more than four decades of gas density, whereas the thermal pressure implies a density (and hence radially) dependent Γ . The same results are obtained for non-radiative simulations without gas cooling and star-formation. We therefore assume that the *total* gas pressure has a polytropic equation of state, $P_{tot} = P_0(\rho/\rho_0)^\Gamma$, where we set $\Gamma = 1 + 1/n = 1.2$ ($n = 5$, where n is the polytropic index) and ρ_0 and P_0 are the central density and pressure of the gas. In Section 2.2.5 we describe our method for including non-thermal pressure in the model and demonstrate that this causes the ratio P_{th}/ρ^Γ to vary with cluster radius.

The final total pressure and density of the gas in our model are given by

$$P_{tot}(r) = P_0 \theta(r)^{n+1} \quad (12)$$

$$\rho_g(r) = \rho_0 \theta(r)^n, \quad (13)$$

where $\theta(r)$ is the polytropic variable

$$\theta(r) = 1 + \frac{\Gamma - 1}{\Gamma} \frac{\rho_0}{P_0} (\Phi_0 - \Phi(r)), \quad (14)$$

and Φ_0 is the central potential of the cluster.

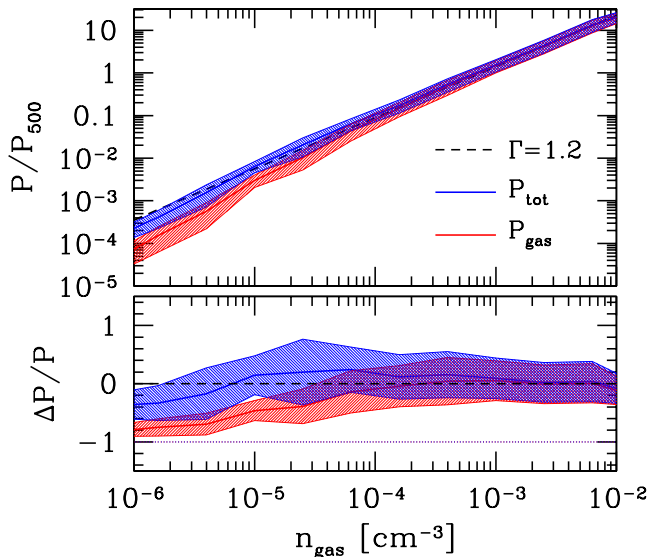


FIG. 1.— Total (blue line) and thermal (red) pressure as a function of gas number density, averaged over 16 clusters simulated by Nagai et al. (2007a) at $z = 0$. The shaded regions show the standard deviation of the cluster sample around the mean. The solid black line shows the best fit line to the total pressure and density with a slope (adiabatic index) of $\Gamma = 1.2$. The lower panel shows the fractional deviation of the pressure around this line.

2.2.4. Energy Feedback

Once P_0 and ρ_0 are determined, the density and pressure profile of the gas is fully specified. These variables are determined by applying two constraints. First, the total final energy of the gas that is initially within R_{vir} must obey

$$E_{g,f} = E_{g,i} + \epsilon_{DM} |E_{DM}| + \epsilon_\ell M_* c^2 + \Delta E_p. \quad (15)$$

This condition states that the final energy $E_{g,f}$ be equal to the initial energy, $E_{g,i}$ (Equation 10), plus energy added to the gas via dynamical process or from energy feedback (discussed below), plus the work done by the gas as it expands or contracts relative to its initial state. We define R_f as the radius within which the final gas mass, following polytropic rearrangement, is equal to $M_{g,i}$ (Equation 9). The work done by the gas is then given by $\Delta E_p = (4\pi/3)(R_{vir}^3 - R_f^3)P_s$. Hence, if $R_f > R_{vir}$ the gas has expanded, doing work in the process. P_s is the surface pressure at R_{vir} , given by $P_s = f_b P_{DM}(R_{vir}) = f_b \sigma_{DM}^2(R_{vir}) \rho_{DM}(R_{vir})$. The surface pressure of the gas at the virial radius is thus equal to that of the dark matter multiplied by the cosmic baryon fraction. The second constraint used to solve the model is that the total pressure of the gas at R_f be equal to the gas pressure at the virial radius of the cluster before polytropic rearrangement, i.e., that $P_{tot}(R_f) = f_b P_{DM}(R_{vir})$.

One fundamental component of the model is the inclusion of heating of the ICM via non-gravitational processes. This can occur via two mechanisms: (1) through energy transfer from the dark matter to gas during major mergers, and (2) via energy feedback from supernovae

and AGN outflows.

To account for the former, Bode et al. (2009) introduced the parameter ϵ_{DM} which controls the fraction of the total dark matter energy, $|E_{\text{DM}}|$, transferred to the ICM during mergers (Pearce et al. 1994; Rasia et al. 2004; Lin et al. 2006; McCarthy et al. 2007). The total dark matter energy is simply the sum of the total dark matter kinetic and potential energy (calculated similarly to Equation 10, but setting $r_* = 0$ and $f_b = 1$). From the hydrodynamical simulations of McCarthy et al. (2007), B09 suggest $\epsilon_{\text{DM}} = 0.05$.

Energy feedback from supernovae or AGNs is assumed, as a first approximation, to be proportional to the total stellar mass of a cluster and is determined by the parameter ϵ_f . The approximate value of this parameter is difficult to determine from hydrodynamical simulations as methods of implementing AGN feedback have only recently started to be investigated in earnest (Sijacki et al. 2007; Di Matteo et al. 2008; Booth & Schaye 2009; Teysier et al. 2010). B09 demonstrated that the feedback parameter can be calibrated by comparing the model to low-redshift X-ray scaling relations, finding values in the range $0 \leq \epsilon_f \leq 1.2 \times 10^{-5}$ depending on assumptions of the stellar mass of clusters and its mass dependence. Recently, Battaglia et al. (2010) investigated the impact of AGN heating in hydrodynamical simulations, finding an effective feedback efficiency (which is roughly equivalent to our ϵ_f) of 5×10^{-6} for an $M_{500} = 6.8 \times 10^{13} h^{-1} M_{\odot}$ cluster over the duration of the simulation.

We note that, in terms of predicting the tSZ power spectrum, the effect of ϵ_f and ϵ_{DM} is somewhat degenerate. Following B09, we take $\epsilon_{\text{DM}} = 0.05$ as our fiducial parameter. In the following section we compare our model using different values of the feedback parameters ϵ_f and ϵ_{DM} with direct X-ray observations of clusters. In Section 4, we investigate the impact of varying both parameters on the SZ power spectrum.

2.2.5. Non-thermal Pressure

Hydrodynamical simulations have demonstrated that a significant fraction of the total energy of the ICM is contained within random gas motions, which provide a significant non-thermal contribution to the total pressure support (Evrard 1990; Rasia et al. 2004; Kay et al. 2004; Dolag et al. 2005; Lau et al. 2009). This kinetic support is largely sourced by infalling and merging structures, which can further generate turbulent gas motions at the boundary between the bulk flow and the thermalized ICM (Dolag et al. 2005; Kim 2007; Vazza et al. 2009). While the level of non-thermal pressure is typically found to be small in the central regions of clusters, it increases steadily with radius, becoming a significant fraction of the total pressure at R_{500} (Lau et al. 2009). The simulation comparison study of Frenk et al. (1999) demonstrated that different hydrodynamics codes predict a similar ratio of kinetic to thermal gas energy in clusters.

To account for non-thermal pressure support in our model, we split the total pressure into non-thermal and thermal components, $P_{\text{tot}}(r) = P_{\text{th}}(r) + P_{\text{nt}}(r)$ and set the non-thermal pressure fraction to be a power law with

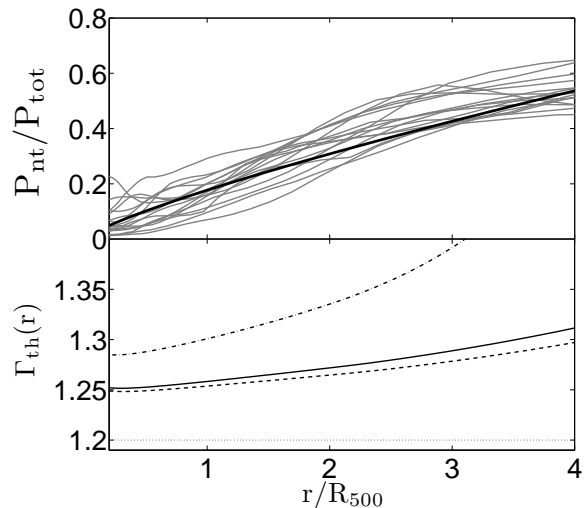


FIG. 2.— **(Upper)** The ratio of non-thermal to total pressure as a function of radius for the 16 simulated clusters of Lau et al. (2009) (gray lines). The thick solid line is the best fit from Equation 16 and represents the fiducial non-thermal pressure fraction assumed in our model. **(Lower)** The thermal polytropic index Γ_{th} (see text) predicted by our gas model as a function of radius. The dotted, solid and dot-dashed black line represents $\alpha_0 = 0, 0.18$ and 0.3 , respectively. The dashed line represents the fiducial model $\alpha_0 = 0.18$, but with no star-formation or feedback.

cluster-centric radius;

$$\frac{P_{\text{nt}}}{P_{\text{tot}}}(z) = \alpha(z) \left(\frac{r}{R_{500}} \right)^{n_{\text{nt}}}, \quad (16)$$

where n_{nt} determines the radial dependence of the non-thermal pressure fraction.

We assume that the non-thermal pressure fraction varies with redshift according to $\alpha(z) = \alpha_0 f(z)$, where α_0 is the mean ratio of non-thermal to total pressure at R_{500} at $z = 0$, and $f(z)$ is a monotonically increasing or decreasing function of redshift. Since $P_{\text{nt}}/P_{\text{tot}} \leq 1$, Equation 16 is valid for $\alpha(z) \leq (R_{\text{max}}/R_{500})^{-n_{\text{nt}}}$. As we describe below, the outermost radius of the pressure profiles in our model is set to $4R_{500}$, which limits the maximum value to $\alpha(z) < 4^{-n_{\text{nt}}}$. We adopt the following form for the redshift evolution,

$$f(z) = \min[(1+z)^\beta, (f_{\text{max}} - 1) \tanh(\beta z) + 1], \quad (17)$$

where $f_{\text{max}} = 4^{-n_{\text{nt}}}/\alpha_0$ and β is a free parameter that determines the evolution rate. This form ensures that, at low redshift ($z < 1$), $\alpha(z)$ has a simple power-law dependence on $(1+z)$, whereas at high redshift (or for large values of α_0) it smoothly asymptotes toward the maximum value of $4^{-n_{\text{nt}}}$. We note that β can be positive or negative. For the former, the value of β controls the redshift of transition from the power law to the asymptotic behavior of $\alpha(z)$. For negative values of β , $\alpha(z)$ declines toward zero with increasing redshift.

We use the hydrodynamical simulations of Nagai et al. (2007a) to find the best-fit values of α_0 and n_{nt} . The upper panel of Figure 2 shows the radial dependence of the ratio of the non-thermal to total gas pressure fraction, $P_{\text{nt}}/P_{\text{tot}}$, of 16 simulated clusters at $z = 0$ (the same set of simulations shown in Figure 1). Following Lau et al. (2009), the non-thermal pressure component

(due to random gas motions) was measured by determining the velocity dispersion of gas cells in radial shells in the rest frame of the cluster. It is clear that the mean non-thermal pressure fraction increases rapidly with radius, from $< 10\%$ at $r = 0.1R_{500}$ to greater than 30% at $r = 2R_{500}$. The thick-solid line indicates the best-fit model with $\alpha_0 = 0.18 \pm 0.06$ and $n_{nt} = 0.8 \pm 0.25$ (resulting in a maximum value of $\alpha(z) = 0.33$). We find no evidence of mass dependence on any of the parameters. Furthermore, Lau et al. (2009) obtained similar results for their non-radiative simulations (i.e., including no cooling or star formation) outside the central regions of the clusters. This indicates that the level of non-thermal pressure is not sensitive to these processes. We note, however, that the preheating simulations of Stanek et al. (2010) do suggest a lower level of kinetic energy in bulk motions than in simulations without preheating.

We determine the redshift dependence by examining a high-redshift output of the simulation. At $z = 1$, we find that the best-fit α_0 increases to 0.26, implying that $\beta \approx 0.5$. A greater fraction of non-thermal pressure towards high redshift is expected due to the increased rate of merger activity in the Λ CDM model. Stanek et al. (2010) also observed an increasing level of kinetic support with redshift in their ‘gravity-only’ smoothed-particle hydrodynamics simulation. However, the results of their preheating simulation imply a decreasing ($\beta < 0$) level of non-thermal pressure toward high redshift. The specific values of α_0 and β predicted by simulations thus appear to be somewhat dependent on the baryonic processes included. We therefore vary these parameters to investigate their impact on the tSZ power spectrum. Further study is required to determine the dependence of non-thermal pressure to cooling and heating effects in hydrodynamical simulations.

We find that n_{nt} decreases by approximately 15% at $z = 1$ compared to the best-fit $z = 0$ value; however, as this change is less than the 0.25 standard deviation on the redshift zero value, we henceforth hold n_{nt} constant with redshift. Our fiducial model is therefore $\alpha_0 = 0.18$, $n_{nt} = 0.8$ and $\beta = 0.5$. We investigate the impact of varying the overall normalization of the profile α_0 and β on the electron pressure profiles of clusters and the tSZ power spectrum, while fixing n_{nt} to the fiducial value for the remainder of the paper. In a future work, we intend to investigate in more detail the mass and redshift dependence of non-thermal pressure profiles in much larger samples of simulated groups and clusters.

The radial thermal pressure profile given by our model is

$$P_{th}(r) = P_o \theta(r)^{n+1} \left[1 - \alpha(z) \left(\frac{r}{R_{500}} \right)^{0.8} \right]. \quad (18)$$

The gas density profile remains as in Equation 13. The radial temperature profile is then given by

$$kT(r) = \mu m_p \frac{P_o}{\rho_0} \theta(r) \left[1 - \alpha(z) \left(\frac{r}{R_{500}} \right)^{0.8} \right], \quad (19)$$

where μ is the mean molecular weight and m_p is the proton mass.

One consequence of including of non-thermal pressure support in our model is that the adiabatic index

of the thermal component of the gas, given by $\Gamma_{th} = \log(P_{th}/P_o)/\log(\rho_g/\rho_o)$, varies as a function of cluster radius. X-ray observations of clusters (Vikhlinin et al. 2006; De Grandi & Molendi 2002) as well as hydrodynamical simulations (Battaglia et al. 2010) indicate that the ICM thermal pressure and density profiles do not adhere to a polytrope with constant index. The lower panel in Figure 2 shows Γ_{th} as a function of radius produced by our model for a $M_{500} = 3 \times 10^{14} h^{-1} M_\odot$ cluster. The solid lines shows the results for $\alpha_0 = 0.18$, the dot-dashed line for $\alpha_0 = 0.30$ and the dotted line for $\alpha_0 = 0$. The dashed line gives the results for $\alpha_0 = 0.18$, but assuming $\epsilon_f = \epsilon_{DM} = M_* = 0$. In the zero non-thermal pressure case, we obtain $\Gamma_{th} = \Gamma = 1.2$, as expected. Setting $\alpha = 0.18$ (0.3) results in a ≈ 5 (8)% increase in Γ_{th} , which also increases with radius. Turning off star formation and feedback in our model reduces this radial dependence slightly.

3. COMPARISON WITH X-RAY OBSERVATIONS

A fundamental test of our model is to compare with the global properties and radial profiles of clusters obtained from X-ray observations. The main aim is to evaluate the range in which the two principal parameters in this model, the feedback parameter ϵ_f and the non-thermal pressure support parameter α_0 , reproduce observed cluster properties. We focus specifically on the $M_{500} - f_g$ relation measured from the cluster samples of Vikhlinin et al. (2006) and Sun et al. (2009) (where the gas fraction f_g is defined as the gas mass divided by total mass within R_{500}), and the ‘universal’ electron pressure profile measured by Arnaud et al. (2010) from the REXCESS cluster sample (Böhringer et al. 2007; Pratt et al. 2009). The latter provides an important test as the radial thermal pressure profile is the cluster property that determines the SZ power spectrum. We have chosen to use the $M_{500} - f_g$ relation as we find the gas fraction in our model to be particularly sensitive to the precise values of ϵ_f .

3.1. Hydrostatic Mass Estimates

One of the principal techniques for measuring cluster masses is to measure the radial gas density and temperature profiles and solve the equation of hydrostatic equilibrium to derive the total mass profile,

$$M(< r) = \frac{-r^2}{G\rho_g} \frac{dP_{tot}}{dr}, \quad (20)$$

(Sarazin 1986; Evrard et al. 1996). However, direct observations of clusters only currently probe the thermal pressure profile and so miss the significant contribution of non-thermal pressure in the ICM. This can result in a systematic underestimation of M_{500} by 10% – 20% (e.g., Rasia et al. 2004; Nagai et al. 2007b; Piffaretti & Valdarnini 2008; Meneghetti et al. 2010). Hence one must take care when comparing simulation or model scaling relations with observations that utilize this technique.

Vikhlinin et al. (2006) and Sun et al. (2009) use this method to measure the masses of the groups and clusters in their sample. Arnaud et al. (2010) determine the mass dependence of the amplitude of the pressure profiles of the clusters in their sample using the $Y_X - M_{500}$ relation calibrated by Vikhlinin et al. (2006). Therefore, in order

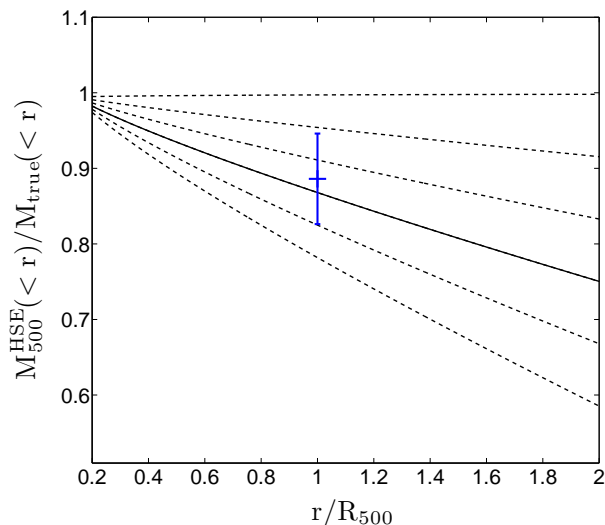


FIG. 3.— Ratio of hydrostatic to true mass measured within spheres of radius r/R_{500} for a cluster of $M_{500} = 3 \times 10^{14} h^{-1} M_{\odot}$. We vary the values of the non-thermal pressure support parameter, $0 \leq \alpha_0 \leq 0.3$ (top to bottom) in steps of 0.06. The solid line represents the fiducial value $\alpha_0 = 0.18$. The blue point represents the mean $M_{500}^{\text{HSE}}/M_{500}$ measured from the simulated clusters of Lau et al. (2009), with the error bar representing the error on the mean.

to compare our model with the observational data, we use the hydrostatic mass predicted by our model M_{500}^{HSE} rather than the true M_{500} .

Figure 3 shows the ratio of hydrostatic to true mass obtained from our model, varying the value of the non-thermal pressure parameter, α_0 from zero (top line) to 0.3 (bottom line) in steps of 0.06. The thick solid line represents our fiducial value of $\alpha = 0.18$. The blue point represents the mean $M_{500}^{\text{HSE}}/M_{500}$ measured from the Lau et al. (2009) simulated clusters, with the error bar representing the error on the mean.

For our fiducial model, M_{500}^{HSE} underestimates the true mass M_{500} by a factor of 0.87 at $r = R_{500}$, increasing to 0.75 at $r = 2R_{500}$. Setting $\alpha_0 = 0.3$ increases this to 0.78 and 0.59 at these radii, respectively. We find that changing the feedback parameter ϵ_f has only a small effect on the hydrostatic mass estimate.

Note that the dependence of M_{500}^{HSE} on α_0 presents a complication in comparing the model with observations as holding M_{500}^{HSE} constant requires varying the true mass M_{500} as we vary the model parameters. This makes it difficult to determine whether changes in predicted properties are due to changes in the true mass or model parameters. To overcome this, in the remainder of this section we fix $M_{500}^{\text{HSE}} = 0.87M_{500}$ (the ratio obtained from our fiducial value of α_0) for all model realizations.

3.2. $M_{500}^{\text{HSE}} - f_g$ relation

In Figure 4, we compare the $M_{500}^{\text{HSE}} - f_g$ relation predicted by our model for different values of ϵ_f against the X-ray observations. The red points are from Vikhlinin et al. (2006), whereas the blue points are from Sun et al. (2009). The solid lines represent the results from our ICM gas model with (from top to bottom) $\epsilon_f = 10^{-7}, 10^{-6}, 5 \times 10^{-6}$, and 10^{-5} . For comparison, we also plot results for $\epsilon_f = \epsilon_{\text{DM}} = 0$ (dashed line) and a maximal

feedback model with $\epsilon_{\text{DM}} = 0.1$, $\epsilon_f = 10^{-5}$ (dot-dashed line). In this plot, α_0 is kept fixed at the fiducial value of 0.18 (note that as we assume a polytropic equation of state between gas density and *total* pressure, changing the non-thermal pressure fraction does not change f_g). The dotted line indicates the cosmic baryon fraction, Ω_b/Ω_M . We have verified that our model predicts $f_g \approx \Omega_b/\Omega_M$ in the absence of star formation and feedback.

It is clear that for high-mass clusters varying the feedback parameter ϵ_f (solid lines) produces little change in the gas fraction. The energy added to the ICM is small compared to the total binding energy for these clusters and thus does not disrupt the gas distribution significantly. However, the impact of energy feedback becomes increasingly important towards lower mass. As cluster mass decreases the feedback energy becomes a larger fraction of the total binding energy. In these systems, feedback has the effect of ‘inflating’ the gas distribution, thus reducing the baryon fraction within a fixed radius.

Setting $\epsilon_{\text{DM}} = 0$ (dashed line) demonstrates that the dark matter energy transfer parameter has a constant effect with mass, reducing f_g by 0.01 – 0.02 across the entire mass range. This is because the energy transferred to the gas from the dark matter is proportional to the binding energy of the cluster, and so has a more significant effect on the high mass clusters than ϵ_f .

There is generally a large amount of intrinsic scatter in the observed sample, especially at the high-mass end where the error bars on individual estimates of f_g are smaller. Although the Vikhlinin et al. (2006) clusters were selected for their relaxed morphology, the large scatter may indicate a range of merger histories within the sample. It may also reflect the large ($\approx 50\%$) intrinsic scatter observed in the mean stellar mass – total mass relation (Giodini et al. 2009; Gonzalez et al. 2007). Nevertheless, the upper and lower model profiles plotted in Figure 4 bracket the observed data points. We therefore assume this range in ϵ_f ($0-10^{-5}$) and ϵ_{DM} ($0-0.1$) when evaluating the modeling uncertainty on the tSZ power spectrum.

3.3. Electron Pressure Profiles

The two key components required to calculate the tSZ power spectrum are the halo mass function and the projected radial electron pressure profiles for clusters over a wide range of mass and redshift. An important test is therefore to compare directly the three-dimensional pressure profiles of our model against those measured from X-ray observations.

Arnaud et al. (2010, henceforth A10) measured the electron pressure profile for intermediate to high-mass ($10^{14} < M_{500}^{\text{HSE}}/M_{\odot} < 10^{15}$), low redshift ($z < 0.2$) clusters in the REXCESS sample (Böhringer et al. 2007; Pratt et al. 2009). The scaling of the amplitude of the profile with cluster mass at R_{500} was found to be $P_e \propto M^{0.69 \pm 0.16}$ and thus in agreement with self-similar expectations ($P_{500} \propto M^{2/3}$, where P_{500} is the characteristic pressure in the self-similar model as described in Appendix A of A10). Due to the low-redshift nature of the REXCESS sample, A10 were not able to constrain significantly the redshift evolution of the sample, assuming that it follows the self-similar form, $P_{500} \propto h(z)^{8/3}$.

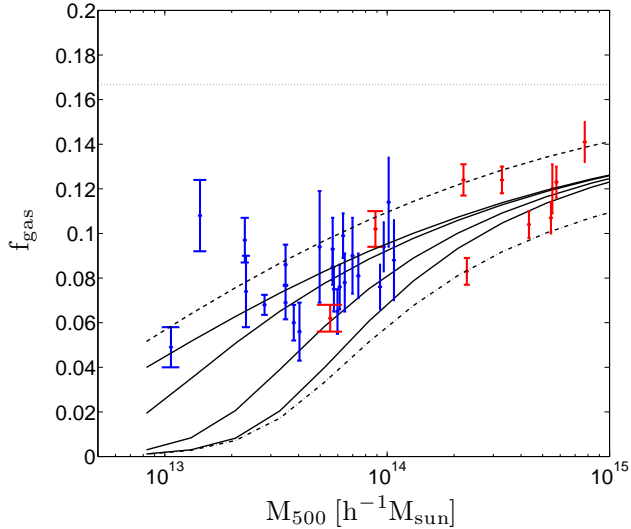


FIG. 4.— Comparison between the observed and model $M_{500}^{\text{HSE}} - f_g$ relation for increasing values of the feedback parameter $\epsilon_f = 10^{-7}, 10^{-6}, 5 \times 10^{-6}$, and 10^{-5} (solid lines, from top to bottom). Points with error bars represent individual cluster observations from Sun et al. (2009) (blue) and Vikhlinin et al. (2009) (red). The dashed line represents the minimal feedback model ($\epsilon_f = \epsilon_{\text{DM}} = 0.0$; i.e., star-formation only). The dot-dashed line is the maximal feedback model with $\epsilon_f = 10^{-5}$ and $\epsilon_{\text{DM}} = 0.1$. The horizontal dotted line represents the universal baryon fraction.

Having rescaled the profiles to remove any mass dependence there was found to be little dispersion (approximately 20%) around the mean profile outside of the core region, $r > 0.2R_{500}$. Within $0.2R_{500}$, A10 observed a much larger dispersion in the measured pressure profiles, with the shape of the profile related to the dynamical state of the cluster. A10 found there to be a good agreement between the observed profiles and those measured from the hydrodynamical simulations of Borgani et al. (2004); Nagai et al. (2007a) and Piffaretti & Valdarnini (2008). As the observations of A10 extend only out to R_{500} , the simulation data were used to extend the best-fit profile out to $4R_{500}$.

3.3.1. Impact of Energy Feedback

In the left panel of Figure 5, we compare the electron pressure profiles for our gas model over a range of values of ϵ_f against the A10 profile. We plot the pressure profiles scaled as $P_e(r)/P_{500}(r/R_{500})^3$ to allow a clear comparison of the profiles in the outer regions, which contribute significantly to the tSZ power spectrum at the angular scales of interest. The solid blue line represents the P09 profile within R_{500} , the radius within which it was observed. The dashed blue line represents the region in which the profile was determined from simulations rather than observations. The shaded region denotes the 20% dispersion observed by A10 around the mean profile. We plot $P_e(r)$ for two different masses, $M_{500}^{\text{HSE}} = 3 \times 10^{14} h^{-1} M_{\odot}$ (black dashed lines) and $M_{500}^{\text{HSE}} = 3 \times 10^{13} h^{-1} M_{\odot}$ (red solid), both at $z = 0.1$. We note that the A10 profile was measured for clusters of mass $M_{500}^{\text{HSE}} > 7 \times 10^{13} h^{-1} M_{\odot}$ and so the lower of the plotted masses represents an extrapolation of the mass dependence of this profile. As in Figure 4, we plot model profiles for $\epsilon_f = 10^{-7}, 10^{-6}, 5 \times 10^{-6}$ and 10^{-5} . α_0 is

fixed at the fiducial value (0.18).

For $M_{500}^{\text{HSE}} = 3 \times 10^{14} h^{-1} M_{\odot}$ (black dashed lines), varying the feedback parameter has a very small effect on the pressure profile, especially within R_{500} . As noted above, for higher mass clusters the feedback energy is a small fraction of the total binding energy and therefore does not strongly influence the gas density and temperature distribution. This is not the case for lower mass clusters. For $M_{500}^{\text{HSE}} = 3 \times 10^{13} h^{-1} M_{\odot}$, increasing the feedback lowers the overall electron pressure within $2R_{500}$, with the effect strongest in the central regions of the cluster. As demonstrated in Figure 4, increasing the feedback parameter has the effect of inflating the gas mass distribution, reducing the gas density within R_{500} and increasing it at larger radii. Although increasing the feedback parameter produces a small rise in gas temperature, this is outweighed by the decrease in the gas density, thus lowering the overall thermal pressure within R_{500} . We note that at larger radii ($r > 1.2R_{500}$), the electron pressure increases with ϵ_f .

For high-mass clusters we find that all values of ϵ_f produce an excellent match to the A10 pressure profile in the range $0.1 \leq r/R_{500} \leq 2$. For $M_{500} = 3 \times 10^{13} h^{-1} M_{\odot}$, a significantly lower mass than any of the observed clusters in the A10 sample, the amplitude of the pressure profile is consistently below that of the A10 profile within R_{500} , but above at larger radii.

3.3.2. Impact of Non-thermal Pressure Support

In the right panel of Figure 5, we show the dependence of the gas model pressure profile on the non-thermal pressure support parameter α_0 . We vary α_0 in range $0 \leq \alpha_0 \leq 0.30$ in steps of 0.06 (from top to bottom at R_{500}). As in the upper panel, the two sets of curves represent clusters of mass $M_{500}^{\text{HSE}} = 3 \times 10^{13}$ and $3 \times 10^{14} h^{-1} M_{\odot}$, respectively. The feedback parameter is fixed at 10^{-6} , which we henceforth take as our fiducial value.

As the fraction of non-thermal pressure support is increased, the profiles become steeper, significantly reducing the thermal pressure in the outer regions. This is entirely expected from Equation 18. For $M_{500}^{\text{HSE}} = 3 \times 10^{14} h^{-1} M_{\odot}$, setting $\alpha_0 = 0.18$ produces a good fit to the A10 profile all the way out to $3R_{500}$. In general, all the values of α_0 explored produce a pressure profile that, for $r < R_{500}$, lies within the 20% dispersion observed around the A10 profile. For $M_{500} = 3 \times 10^{13} h^{-1} M_{\odot}$ the profiles tend to lie below the A10 profile within R_{500} , but predict a higher pressure beyond this radius.

3.3.3. Mass and Redshift Dependence

At $r = R_{500}$, our fiducial model ($\epsilon_f = 10^{-6}$ and $\alpha_0 = 0.18$) produces a mass scaling of $P_e(R_{500}) \propto M^{0.75 \pm 0.01}$. At $0.5R_{500}$, this steepens to $M^{0.79 \pm 0.01}$. This steepening of the mass scaling at smaller radii was also observed by A10, who found a scaling of $M^{0.69 \pm 0.16}$ and $M^{0.78 \pm 0.16}$ at $r = R_{500}$ and $0.5R_{500}$, respectively⁶.

In Figure 6, we plot the redshift evolution of the pressure profile where the solid, dashed, dot-dashed, and dotted lines correspond to $z = 0, 0.5, 1$ and 2 , respectively.

⁶ We assume the same error on the mass scaling at $0.5R_{500}$ as was measured at R_{500} for the A10 profile.

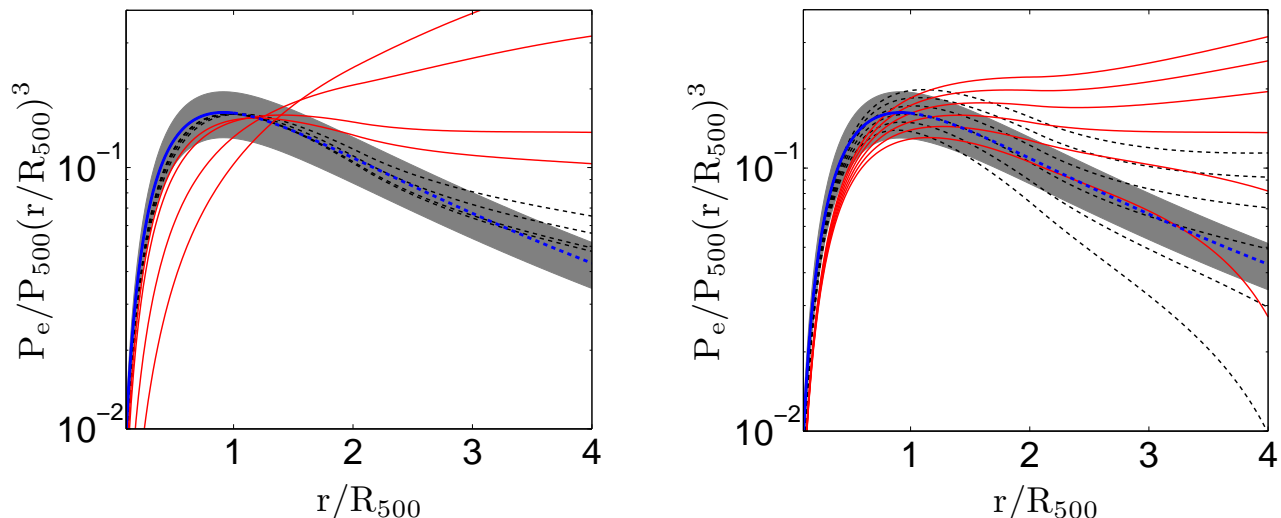


FIG. 5.— **(Left)** Electron pressure profiles for clusters of mass $M_{500}^{\text{HSE}} = 3 \times 10^{14} h^{-1} M_{\odot}$ (black dashed lines) and $M_{500}^{\text{HSE}} = 3 \times 10^{13} h^{-1} M_{\odot}$ (red lines), using feedback parameters values of $\epsilon_f = 10^{-7}, 10^{-6}, 5 \times 10^{-6}$, and 10^{-5} (from bottom to top at $2R_{500}$). The blue line represents the A10 pressure profile, with the shaded region denoting the observed 20% dispersion around this profile. **(Right)** Same as the upper panel but for increasing values of the non-thermal pressure support parameter $0 \leq \alpha_0 \leq 0.30$ in steps of 0.06 (from top to bottom)

The blue lines represent the A10 profiles at each redshift, for which the normalization is assumed to scale self-similarly, i.e., $P_{500} \propto h(z)^{2.67}$.

At $r \approx 1.5R_{500}$ our model reproduces the self-similar scaling of the A10 profile, but scales differently with redshift at smaller and larger radii. As redshift increases, the profile becomes more centrally concentrated, with the pressure increasing with respect to the A10 profile for $r \leq 1.5R_{500}$, but decreasing at larger radii. At $r = 0.5, 1$ and $2R_{500}$ we find that the profile scales as $\propto h(z)^{2.71 \pm 0.04}$, $h(z)^{2.79 \pm 0.05}$ and $h(z)^{2.57 \pm 0.06}$.

There are three components of our fiducial model that evolve with redshift at fixed halo mass: the stellar mass fraction M_*/M_{500} (and thus the feedback energy), halo concentration – both of which decrease towards increasing redshift – and the non-thermal pressure parameter α , which initially increases as $(1+z)^{0.5}$ but asymptotes toward an upper limit of $\alpha(z) = 0.33$ at high redshift (Section 2.2.5). While the increasing non-thermal pressure support produces a negative redshift evolution, this is compensated to some extent by the decreasing concentration. At fixed mass, as halo concentration decreases so does the central gravitational potential, reducing the pressure in the inner regions as well as increasing it at larger radii. We find that removing the redshift evolution of the concentration parameter (Equation 6) results in a significant weakening of the redshift evolution relative to self-similar, $P_e(2R_{500}) \propto h(z)^{1.84 \pm 0.05}$. However, the evolving stellar mass fraction does not have a strong effect on the redshift scaling of the pressure profiles.

4. SUNYAEV-ZEL'DOVICH ANGULAR POWER SPECTRUM

The primary goal of this work is to investigate the variations in the predicted tSZ power spectrum caused by uncertainties in ICM physics, in this case parameterized by the energy feedback and non-thermal pressure support parameters described in Sections 2.2.4 and 2.2.5. In the previous section we demonstrated the effect of varying

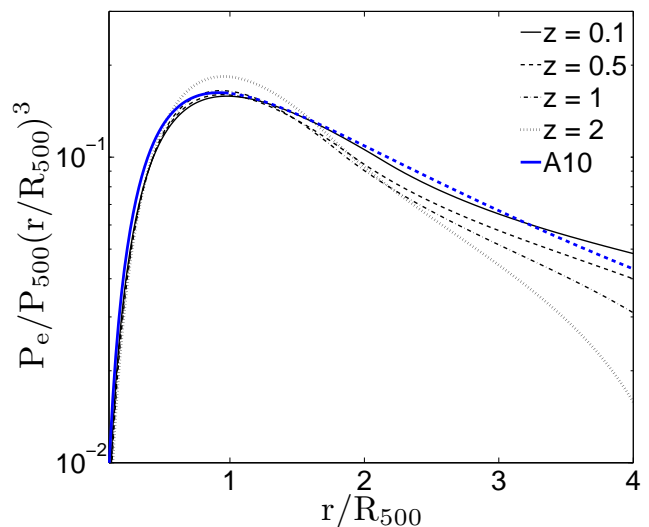


FIG. 6.— Pressure profiles for model clusters at different redshifts, where $z = 0, 0.5, 1$, and 2 (solid, dashed, dot-dashed, dotted and thin solid lines, respectively). The blue line is the observed pressure profile of A10. The cluster mass is fixed at $M_{500}^{\text{HSE}} = 3 \times 10^{14} h^{-1} M_{\odot}$.

these parameters on the pressure profile for individual clusters, comparing with results from high-quality X-ray cluster observations. We now repeat this exercise for the tSZ power spectrum. We also compare our fiducial model with previous simulations or models and the recent SPT observations of the tSZ power spectrum.

4.1. Impact of Cluster Physics

Figure 7 illustrates the tSZ power spectrum obtained while varying the energy feedback parameters (ϵ_f and ϵ_{DM}), the normalization of the halo mass-concentration relation (A_C), the non-thermal pressure support param-

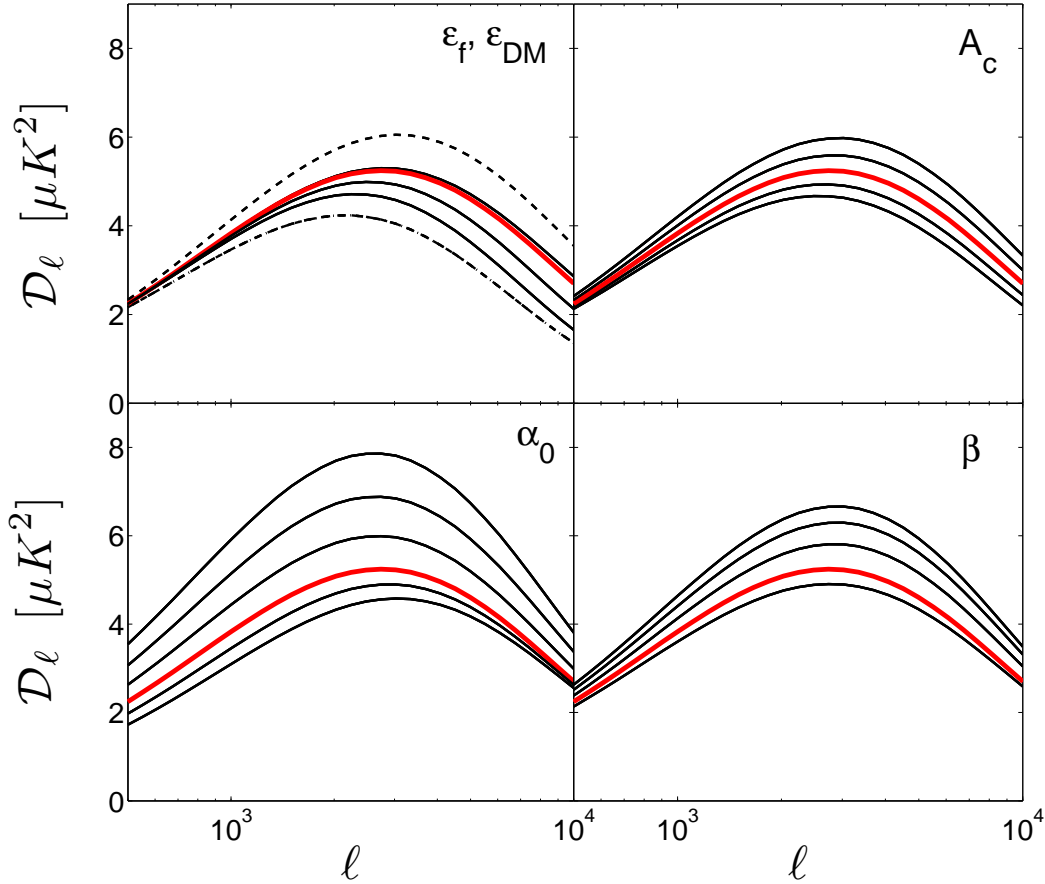


FIG. 7.— **(top, left)** The tSZ power spectrum for different values of ϵ_f and ϵ_{DM} . At $\ell = 10,000$, the values of ϵ_f are (from top to bottom) 10^{-7} , 10^{-6} , 5×10^{-6} and 10^{-5} . The dashed line denotes $\epsilon_{DM} = \epsilon_f = 0$. The dot-dashed line indicates a model with $\epsilon_f = 10^{-5}$ and $\epsilon_{DM} = 0.1$. **(top, right)** tSZ power spectrum for different normalizations of the halo concentration-mass relation. At $\ell = 10,000$, $A_C = 0.8, 0.9, 1.0, 1.1, 1.2$. (from bottom to top) **(bottom, left)** tSZ power spectrum for increasing values of α_0 , where, from top to bottom, $0 \leq \alpha_0 \leq 0.30$ in steps of 0.06. **(bottom, right)** Varying the value of the non-thermal pressure support redshift evolution parameter β in the range $-1 \leq \beta \leq 1$ (from top to bottom) in steps of 0.5. In each case, the thick red line represents our fiducial model.

Value	ϵ_f	ϵ_{DM}	α_0	β	A_C
Fiducial	10^{-6}	0.05	0.18	0.5	1.0
Min.	0	0	0	-1	0.8
Max.	10^{-5}	0.1	0.3	1	1.2

TABLE 1
RANGE OF GAS MODEL PARAMETERS.

eter (α_0) and its redshift dependence (β). In each plot, the thick red line denotes the power spectrum obtained from our fiducial model parameters. Table 1 summarizes the fiducial, maximum and minimum of each parameter explored. The range within which we vary α_0 , ϵ_f and ϵ_{DM} are chosen such that our model brackets the observations described in the previous section.

We plot the band powers in terms of $\mathcal{D}_\ell = \ell(\ell + 1)C_\ell/(2\pi)$ in units of μK^2 at 147 GHz (i.e., $f(x_\nu) = -1$ in Equation 2). Note that we truncate our model profiles at $2R_{vir} (\approx 4R_{500})$. This radius was chosen to roughly coincide with that of the accretion shock that is observed in hydrodynamical simulations (e.g., Molnar et al. 2009). We do not expect our model to be valid beyond the shock radius. Furthermore, the contribution of the low-density

gas outside of groups and clusters to the tSZ power spectrum is expected to be small (Hallman et al. 2009; Trac et al. 2010). Nevertheless, by doubling (tripling) the outermost radius we find an average increase of only 6% (7%) in tSZ power.

In the top-left panel, we plot the tSZ power spectrum varying the feedback parameter between $\epsilon_f = 10^{-7}, 10^{-6}, 5 \times 10^{-6}$ and 10^{-5} (solid lines from top to bottom at $\ell = 10,000$). The dashed line represents $\epsilon_f = \epsilon_{DM} = 0$ and the dot-dashed line $\epsilon_f = 10^{-5}, \epsilon_{DM} = 0.1$. Increasing ϵ_f and ϵ_{DM} has the effect of suppressing power at small angular scales, causing \mathcal{D}_ℓ to peak at increasingly large scales. For example, for $\epsilon_f = \epsilon_{DM} = 0$, \mathcal{D}_ℓ peaks at $\ell = 3000$, while for the largest feedback values probed, \mathcal{D}_ℓ peaks at $\ell = 2000$. Similar results have recently been reported by Battaglia et al. (2010), who investigate the impact of AGN feedback in hydrodynamical simulations on the SZ power spectrum. The suppression of small-scale power is caused by the inflating effect of energy feedback flattening the pressure profiles in the inner regions of clusters. As demonstrated in Figure 5, increasing feedback has the strongest effect on lower mass clusters $M < 10^{14} h^{-1} M_\odot$, which principally contribute

to the power spectrum on small angular scales.

In the lower-left panel of Figure 7, we show the tSZ power spectrum for increasing values of the non-thermal pressure parameter, α_0 . We increase α_0 in steps of 0.06 between 0 and 0.30 (from top to bottom at $\ell = 1000$), while holding the other gas model parameters at their fiducial value.

Increasing α_0 results in a significant decrease in power, particularly at large angular scales; at $\ell = 3000$, the full range in α_0 encompasses more than a factor of 2 in power. In Section 3.3 we demonstrated that increasing the non-thermal pressure parameter significantly decreases the thermal pressure at large radii. This drives the large reduction in tSZ power, particularly at low ℓ . We note that for higher values of α_0 , $\alpha(z)$ rapidly reaches the maximum value of 0.33 for the fiducial value of $\beta = 0.5$. The effect of increasing α_0 therefore begins to saturate for $\alpha_0 > 0.18$. This is particularly noticeable on small scales ($\ell \geq 5000$), where high redshift groups and clusters contribute significantly. It is evident that determining the level of non-thermal pressure support in groups and clusters, from all sources, is important in predicting the amplitude of their tSZ signal.

In the lower-right panel of Figure 7, we plot (from top to bottom) the tSZ power spectrum for $\beta = -1, -0.5, 0, 0.5$ and 1. We hold α_0 fixed at 0.18. It is clear that the largest absolute change in power is at $\ell = 2500$, although the fractional change is similar across the full range of angular scales plotted. This is in contrast to varying α_0 , which produces an increasing effect toward lower ℓ . The reason for this is that varying β predominantly affects high redshift objects, which contribute to the tSZ power spectrum at smaller angular scales than lower redshift objects of the same mass. However, α_0 primarily influences the pressure profiles at large radii (i.e., larger angular scales). Hence, there is a trade-off with the largest change in power being found at intermediate scales.

In the upper-right panel we plot the tSZ power spectrum while varying the normalization of the mass-concentration relation around the Duffy et al. (2008) value. This is achieved by setting $A_C = 0.8, 0.9, 1.0, 1.1$ and 1.2 (from bottom to top at $\ell = 10,000$), where A_C is defined in Equation 6. The results show that increasing halo concentration boosts the SZ power at small angular scales. For a given mass, higher concentration halos have a deeper central potential, thus increasing the pressure required for the inner regions of clusters to maintain gas in hydrostatic equilibrium. This steepens the pressure profiles in the inner regions of clusters, resulting in the observed increase in power at small angular scales. It is interesting to note that the impact of varying A_C on the tSZ power spectrum is somewhat similar to that of varying the feedback parameter ϵ_f .

4.2. Comparisons with Simulations

In Figure 8, we compare our model to other recent models or simulations. When comparing with simulations, we plot both our fiducial model (dashed lines) and a second realization in which we adjust the model parameters to match the physics assumed in each simulation (dot-dashed lines), for example, by turning off star formation and energy feedback. This enables us to examine the impact of second-order cluster properties (such as

morphology and substructure) that are not accounted for in our halo-model approach.

In the top-left panel we compare our model with the simulations of Sehgal et al. (2010), who calculated the SZ power spectrum using simulated SZ sky maps generated by applying the semi-analytic model of Bode et al. (2009) to halos identified in an N-body lightcone simulation. This approach thus includes the effects of variations in halo density profiles, scatter in the mass-concentration relation and halo morphology (although the requirement of hydrostatic equilibrium will suppress the impact of substructure). The key difference between the model of Bode et al. (2009) and that described here is our inclusion of radially dependent non-thermal pressure support. The dot-dashed line demonstrates that we are able to reproduce almost exactly the Sehgal et al. (2010) tSZ power spectrum when we set $\alpha_0 = 0$. This implies that variations in dark matter halo structural properties, do not strongly affect the tSZ power spectrum at the angular scales investigated here. Comparing the Sehgal et al. (2010) prediction with our fiducial model highlights the importance of incorporating non-thermal pressure support in ICM gas models.

In the top-right panel, we compare our fiducial power spectrum with that predicted by the model of Komatsu & Seljak (2002). This model also assumes that the ICM is in hydrostatic equilibrium, but does not include star formation or any non-gravitational heating mechanisms. While it is difficult to isolate the exact cause of the difference between the two profiles, Battaglia et al. (2010) have recently demonstrated the Komatsu & Seljak (2002) model significantly over-predicts the thermal gas pressure at large radii in comparison to observations, which is consistent with the factor of 2 increase in power compared to our model.

In the lower-left panel we compare our model with SZ power spectra measured from recent hydrodynamical simulations. The red-solid line shows the non-radiative, GADGET-2 simulation of Battaglia et al. (2010), and the red-dashed line shows the result of a rerun of this simulation including cooling, star formation and AGN feedback. The dotted lines show the expected sample variance around the non-radiative simulation given the simulated map size ($1.6^\circ \times 1.6^\circ$, see also Shaw et al. 2009). The black dashed line shows our fiducial model. For comparison, we also plot our model prediction having set the stellar mass and feedback energy to zero (black, dash-dotted line).

The simulation without star formation, cooling and feedback predicts a higher tSZ signal than the one that includes these processes. On small scales, this is principally due to the suppression of the SZ signal in the central regions of lower mass structures as gas is expelled by AGNs (Battaglia et al. 2010). On larger scales the difference is driven by the lower gas mass in clusters due to star formation. Our model without star formation or feedback demonstrates reasonable agreement with the non-radiative simulation at intermediate scales ($\ell \approx 4000$). However, at larger scales it lies systematically above the simulation, and below at smaller scales. The latter may be due to additional power in the simulation power spectrum due to the presence of substructures. The difference at large scales is most likely due to an artificial suppression in the abundance of the most massive clusters due

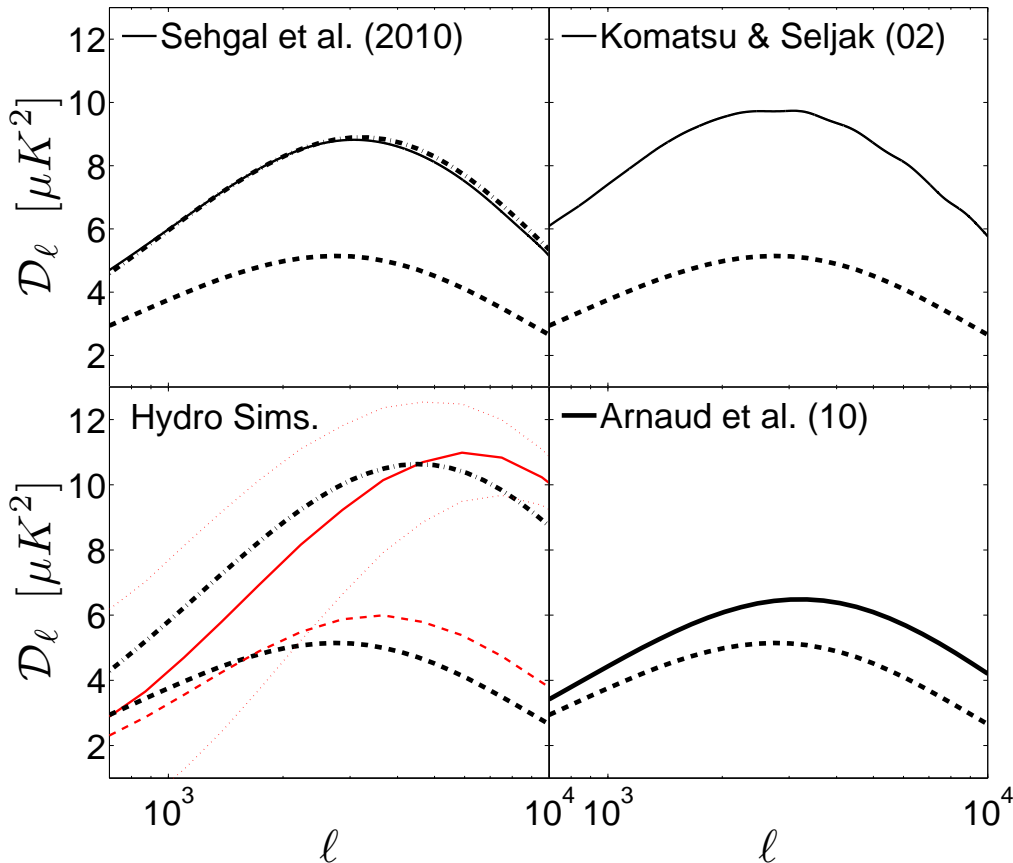


FIG. 8.— Comparison with simulations and other models (solid lines). In each panel, the black dashed line is our fiducial model and the dash-dot line our model having modified the input parameters to reflect the level of physics incorporated in the simulation (where applicable). In the lower-left panel, the red lines show the results of the hydrodynamical simulations of Battaglia et al. (2010). All results are plotted at 147 GHz and are scaled to $\sigma_8 = 0.8$ and $\Omega_M = 0.264$.

to the limited simulation volume.

We find that our fiducial model matches that of the AGN simulation at $\ell = 1800$, but, as with the non-radiative simulation, produces more power at larger scales and less at smaller scales. We note that by increasing the amplitude of the mass-concentration relation by 20% our model very nearly reproduces the Battaglia et al. (2010) simulations for $\ell > 3000$. The overall reduction between the cases with and without baryon cooling and feedback are similar for the model and simulations. This indicates that the feedback prescriptions incorporated in our fully analytic model are able to reproduce the results of sub-grid models of AGN feedback in (computationally intensive) hydrodynamical simulations.

Finally, in the lower-right panel we compare our fiducial model with that predicted by the Arnaud et al. (2010) pressure profile. Our model lies below that inferred by the Arnaud et al. (2010) profile, particularly at small scales. As shown in Figure 5, group-mass objects have a significantly lower pressure at small radii ($r < R_{500}$) in our model compared to the A10 profile, which results in less power at small angular scales. By reducing the level of non-thermal pressure support in our model by one third (i.e. $\alpha_0 = 0.12$) and setting the redshift evolution of this parameter to zero our model will produce a power spectrum very similar to that of the

Arnaud et al. (2010) profile.

4.3. Comparisons with Observations

The current generation of SZ surveys (SPT, ACT and Planck) have the necessary combination of sensitivity, angular resolution, mapping speed and frequency coverage to make precise measurements of the tSZ power spectrum. Multifrequency observations are important for measuring the tSZ amplitude as both radio point sources and dusty star-forming galaxies (DSFGs) provide significant foreground signals near 150 GHz. While the Poisson component of these point source populations has a different angular dependence to the SZ signal and can thus be separated and removed, the distribution of DSFGs on the sky are expected to be clustered with a power spectrum of similar shape to the SZ signal (Viero et al. 2009; Hall et al. 2010). Hence, for single frequency surveys, the clustered DSFG and SZ power spectra cannot be distinguished. Fortunately, the spectral dependence of these signals differs greatly and thus observing at two frequencies allows the clustered DSFG and SZ components to be separated. With three frequencies the kinetic and tSZ signals can also be independently measured.

In Figure 9, we compare our fiducial model of the tSZ power spectrum to the recent SPT measurements of the small-scale CMB power spectrum. In this figure, the blue

points with error bars represent the DSFG-subtracted power spectrum measured by Lueker et al. (2010). This was obtained by combining the maps at 220 and 150 GHz to optimally remove the point source signal. The resulting DSFG-subtracted power spectrum has been rescaled (by a factor of 2.2) to preserve the amplitude of the primary CMB signal (see Section 6.2 of Lueker et al. 2010). Therefore, in order to enable a comparison with the observations we have multiplied the tSZ power spectrum calculated with our model by this same factor. The dashed black line is the best-fit CMB+tSZ+kinetic SZ (kSZ) model (plus a residual point source component) to the SPT observations assuming no theoretical uncertainty in the SZ predictions. Lueker et al. (2010) adopted the simulations of Sehgal et al. (2010) to infer a value of $\sigma_8 = 0.746$ from this fit (i.e., from the amplitude of the tSZ power spectrum alone). The solid and dashed red lines are the tSZ power spectrum predictions for our fiducial gas model parameters for $\sigma_8 = 0.8$ and $\sigma_8 = 0.775$, respectively (keeping the primary CMB, kSZ and point source components fixed). As in Lueker et al. (2010), we use the ‘homogeneous’ kinetic SZ power spectrum of Sehgal et al. (2010).

Figure 9 demonstrates that our fiducial model matches the best-fit SPT power spectrum (dashed black line) when we lower σ_8 to 0.775, reducing the discrepancy with the WMAP inferred value and constraints from cluster abundances. Increasing the values of α_0 , ϵ_f or ϵ_{DM} would increase the value of σ_8 derived from the SPT measurements further. In general, we find that our fiducial model scales as $C_\ell \propto \sigma_8^{8.4}$ (at $\ell = 3000$), which is steeper than the power of seven scaling found by Komatsu & Seljak (2002). This is due to the larger fractional contribution of higher mass objects to the tSZ power at these scales in our model, the abundance of which is extremely sensitive to the value of σ_8 .

5. DISCUSSION AND CONCLUSION

The primary goal of this paper is to investigate the level of theoretical uncertainty on the amplitude of the tSZ angular power spectrum due to uncertainties in the physics of the ICM. To this end, we have developed an analytic model for the pressure and density distribution of the ICM. Our model is based on that of Ostriker et al. (2005) which assumes the ICM resides in hydrostatic equilibrium in the potential well of NFW halos with a polytropic equation of state. The model accounts for star formation, energy feedback and energy transfer from dark to gas during mergers. We have made a significant improvement to the model by accounting for non-thermal pressure support in the ICM due to random gas motions, calibrating the non-thermal pressure profile from hydrodynamical simulations. This method allows us to rapidly generate theoretical thermal SZ power spectra, enabling a thorough investigation of the relative impact of astrophysical and cosmological parameters and their degeneracies.

Our model has four key free parameters: an energy feedback parameter ϵ_f , which determines the amount of non-gravitational heating of the ICM from supernovae or AGNs, a dark-matter energy transfer parameter ϵ_{DM} , which governs the energy exchanged from dark matter to gas during mergers, a non-thermal pressure support parameter, α_0 , which gives the level of non-thermal pres-

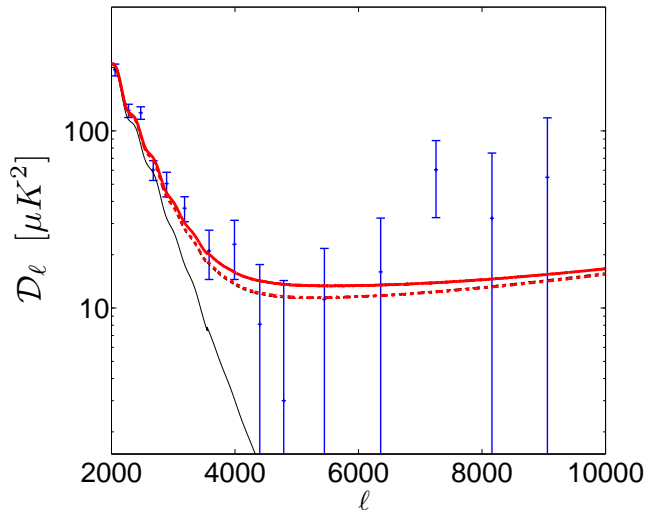


FIG. 9.— Comparisons with SPT measurements of the CMB power spectrum at small angular scales. The blue points with error bars are the DSFG-removed power spectrum measured by SPT, multiplied by 2.2 to preserve the amplitude of the primary CMB power spectrum (see text). The dashed black line is the best-fit CMB+tSZ+kSZ model to the SPT results. The red solid line is our fiducial tSZ model (plus primary CMB, kSZ and residual point sources) with $\sigma_8 = 0.8$, the red dashed line is our fiducial model with $\sigma_8 = 0.775$ (almost directly on top of the black-dashed line). Results are at 153 GHz. The thin black line is WMAP5 best-fit primary CMB temperature anisotropy power spectrum.

sure at $z = 0$ and its redshift evolution. These parameters were calibrated against low redshift X-ray observations of groups and clusters, including the $M_{500} - f_g$ (gas fraction) relation (Vikhlinin et al. 2006; Sun et al. 2009) and observed electron pressure profiles (Arnaud et al. 2010). These studies derive mass estimates for observed clusters using the equation of hydrostatic equilibrium, which simulations suggest underestimate true cluster mass by 10% – 20%. Therefore, to ensure a consistent comparison, we are careful to use the hydrostatic (rather than true) mass predicted by our model when comparing with observations.

We have found that increasing the energy feedback parameter, ϵ_f , from 10^{-7} to 10^{-9} has little effect on the pressure and density of high-mass clusters (where feedback energy is a small fraction of the total binding energy), but produces a factor of 2 decrease in the gas fraction for group mass objects. Similarly, increasing the feedback energy dramatically reduces the gas pressure within R_{500} and increases the pressure at larger radii in groups. Raising the level of non-thermal pressure (i.e., increasing α_0) steepens the pressure profiles significantly in the outer regions ($r \geq R_{500}$) of both groups and clusters. We found that a fiducial model of $\epsilon_f = 10^{-6}$ and $\alpha_0 = 0.18$ provides an excellent fit to the thermal pressure profile observed by A10.

By combining our gas model with the halo mass function, we investigated the impact of varying the energy feedback, non-thermal pressure support and its redshift evolution on the tSZ power spectrum. We also evaluated the effect of perturbing the normalization of the mass-concentration relation in our model around the mean relation reported by Duffy et al. (2008). We found that increasing ϵ_f (and ϵ_{DM}) suppresses power on small angu-

lar scales, but does not strongly affect large-scale power. Hence, the peak of the power spectrum shifts to larger angular scales as we increase the amount of energy feedback. This is because ϵ_f has a more significant effect on lower mass systems, which primarily contribute power on small scales. Varying the normalization of the mass-concentration relation A_C has a somewhat similar effect; the power on small scales increases with A_C . Raising the concentration of the host halo deepens the central potential and thus steepens the gas pressure profile so as to maintain hydrostatic equilibrium.

Varying the non-thermal pressure parameter α_0 has the opposite effect to the feedback parameters; increasing α_0 strongly suppresses power on intermediate and large scales ($\ell < 5000$). The peak of the power spectrum shifts slightly to smaller scales as α_0 is increased. Generally, we found that non-thermal pressure support, at the level observed in recent hydrodynamical simulations, has a significant effect on the tSZ power spectrum, reducing the amplitude by a factor of 2 relative to the thermal pressure-only case.

We have demonstrated that our model reproduces the tSZ power spectrum measured from simulated maps constructed by applying the semi-analytic model of Bode et al. (2009) to halos identified in an N-body lightcone simulation (Sehgal et al. 2010). This demonstrates that deviations in halo structural properties (such as scatter in the mass-concentration relation) do not strongly affect the tSZ power spectrum, justifying our halo model-based approach. However, comparing with hydrodynamical simulations demonstrates that analytic models may potentially miss some small scale power due to substructures in simulations. A more detailed comparison of hydrodynamical simulations with semi-analytic models is required to isolate the impact of second order cluster properties on the SZ power spectrum.

Recent SPT measurements of the small-scale CMB temperature anisotropy power spectrum (Lueker et al. 2010) have demonstrated there to be some tension between the value of σ_8 implied by the measured amplitude of the tSZ power spectrum at $\ell = 3000$ and those derived from WMAP observations of the primary CMB power spectrum (Dunkley et al. 2009; Komatsu et al. 2010), or from cluster abundances (Vikhlinin et al. 2009; Mantz et al. 2010). This tension can be alleviated if the simulations used by Lueker et al. (2010) overestimate the amplitude of the SZ power spectrum by approximately a factor of 2. When compared with the SPT results, we found that our fiducial model infers $\sigma_8 = 0.775$, and thus reduces the discrepancy in the value of σ_8 between this and other probes. Generally, we find that our fiducial model scales as $C_\ell \propto \sigma_8^{8.4}$.

The results presented by Lueker et al. (2010) encompasses roughly 5% of the expected SPT final survey area. Over the next few years, SPT, ACT and Planck should produce precise measurements of the SZ power spectrum amplitude over a wide range of angular scales $2000 \leq \ell \leq 10,000$. We have demonstrated that physics in cluster environments can modify the shape of the power spectrum, as well as the amplitude. By comparing the ratio of power measured at small, intermediate and

larger scales it should be possible to derive information regarding the relative influence of feedback processes and non-thermal pressure support in the ICM (albeit over a wide range of mass and redshift). Given that a significant fraction of SZ power derives from high-redshift and low-mass objects, the tSZ power spectrum can provide an exciting tool for studying the state of gas in these objects.

From a theoretical perspective, several improvements can be made to our modeling of the ICM. First, our prescription assumes feedback from supernovae and AGNs is even distributed into the ICM. Although a concerted effort to implement and study AGN feedback in hydrodynamical simulations of cosmological volumes has only recently begun (Sijacki et al. 2007; Di Matteo et al. 2008; Booth & Schaye 2009; Teyssier et al. 2010), these studies will shed light on the extent to which non-gravitational heating sources are able to influence the thermal structure of the ICM. While our model accounts for energy transfer between dark matter and gas during mergers, the efficiency with which the process occurs has been poorly studied in simulations. Furthermore, we have not accounted for any uncertainty in the slope and amplitude of the stellar mass – total mass relation used in our model, which is poorly constrained at higher redshifts. Finally, the evolution of the radial, mass and redshift dependence of non-thermal pressure support (from any source) needs to be studied in hydrodynamical simulations in more detail. Future X-ray observatories equipped with high-resolution calorimeters (such as ASTRO-H) will provide important constraints on the non-thermal pressure support due to internal gas motions via broadening of heavy ion emission lines.

In this paper, we have not studied the degeneracies in our model between astrophysical and cosmological parameters in the shape and amplitude of the tSZ power spectrum, and how these may limit the precision to which σ_8 , for example, can currently be constrained in this way. We leave this to a follow-up paper (Bhattacharya et al. 2010b). However, our prescription allows the observed shape of the power spectrum to be used to weaken or break some of these degeneracies. Alternatively, one can marginalize over the feedback or non-thermal pressure parameters in our model in order to account for astrophysical uncertainty in the predicted tSZ power spectrum. We intend to make the code for our model publicly available for use in analyzing observations of the small-scale CMB power spectrum.

6. ACKNOWLEDGMENTS

We thank Gus Evrard, Gil Holder, Jerry Ostriker, Klaus Dolag, Douglas Rudd, Christian Reichardt and Alexey Vikhlinin for useful discussions. We also thank Nicholas Battaglia for making the results of his cosmological hydrodynamics simulations available to us. LS and DN acknowledge the support of Yale University and NSF grant AST-1009811. SB acknowledges support from the LDRD and IGPP program at Los Alamos National Laboratory. This work was supported in part by the facilities and staff of the Yale University Faculty of Arts and Sciences High Performance Computing Center.

REFERENCES

- Bhattacharya, S., Heitmann, K., White, M., Lukić, Z., Wagner, C., & Habib, S. 2010a, ArXiv e-prints
- Bhattacharya, S., Shaw, L., & Nagai, D. 2010b, in prep.
- Birkinshaw, M. 1999, *Physics Reports*, 310, 97
- Bode, P., Ostriker, J. P., & Vikhlinin, A. 2009, *ApJ*, 700, 989
- Böhringer, H., Schuecker, P., Pratt, G. W., & et al. 2007, *A&A*, 469, 363
- Booth, C. M. & Schaye, J. 2009, *MNRAS*, 398, 53
- Borgani, S., Murante, G., Springel, V., Diaferio, A., Dolag, K., Moscardini, L., Tormen, G., Tornatore, L., & Tozzi, P. 2004, *MNRAS*, 348, 1078
- Bracewell, R. N. 2000, *The Fourier transform and its applications*, ed. Bracewell, R. N.
- Bryan, G. L. & Norman, M. L. 1998, *ApJ*, 495, 80
- Carlstrom, J. E., Holder, G. P., & Reese, E. D. 2002, *ARA&A*, 40, 643
- Dawson, K. S., Holzapfel, W. L., Carlstrom, J. E., Joy, M., & LaRoque, S. J. 2006, *Astrophys. J.*, 647, 13
- De Grandi, S. & Molendi, S. 2002, *ApJ*, 567, 163
- Di Matteo, T., Colberg, J., Springel, V., Hernquist, L., & Sijacki, D. 2008, *ApJ*, 676, 33
- Dolag, K. & Staszczyn, F. 2009, *MNRAS*, 398, 1678
- Dolag, K., Vazza, F., Brunetti, G., & Tormen, G. 2005, *MNRAS*, 364, 753
- Duffy, A. R., Battye, R. A., Davies, R. D., Moss, A., & Wilkinson, P. N. 2008, *MNRAS*, 383, 150
- Dunkley, J., Komatsu, E., Nolta, M. R., Spergel, D. N., Larson, D., Hinshaw, G., Page, L., Bennett, C. L., Gold, B., Jarosik, N., Weiland, J. L., Halpern, M., Hill, R. S., Kogut, A., Limon, M., Meyer, S. S., Tucker, G. S., Wollack, E., & Wright, E. L. 2009, *ApJS*, 180, 306
- Evrard, A. E. 1990, *ApJ*, 363, 349
- Evrard, A. E., Metzler, C. A., & Navarro, J. F. 1996, *ApJ*, 469, 494
- Fowler, J. W., Acquaviva, V., Ade, P. A. R., Aguirre, P., & et al. 2010, *ApJ*, 722, 1148
- Frenk, C. S., White, S. D. M., Bode, P., Bond, J. R., Bryan, G. L., Cen, R., Couchman, H. M. P., Evrard, A. E., Gnedin, N., Jenkins, A., Khokhlov, A. M., Klypin, A., Navarro, J. F., Norman, M. L., Ostriker, J. P., Owen, J. M., Pearce, F. R., Pen, U., Steinmetz, M., Thomas, P. A., Villumsen, J. V., Wadsley, J. W., Warren, M. S., Xu, G., & Yepes, G. 1999, *ApJ*, 525, 554
- Friedman, R. B. & QUaD Collaboration. 2009, in *American Astronomical Society Meeting Abstracts*, Vol. 213, American Astronomical Society Meeting Abstracts, 340.06+
- Giodini, S., Pierini, D., Finoguenov, A., Pratt, G. W., Böhringer, H., Leauthaud, A., Guzzo, L., Aussel, H., Bolzonella, M., Capak, P., Elvis, M., Hasinger, G., Ilbert, O., Kartaltepe, J. S., Koekemoer, A. M., Lilly, S. J., Massey, R., McCracken, H. J., Rhodes, J., Salvato, M., Sanders, D. B., Scoville, N. Z., Sasaki, S., Smolcic, V., Taniguchi, Y., Thompson, D., & the COSMOS Collaboration. 2009, *ApJ*, 703, 982
- Gonzalez, A. H., Zaritsky, D., & Zabludoff, A. I. 2007, *ApJ*, 666, 147
- Hall, N. R., Keisler, R., Knox, L., Reichardt, C. L., Ade, P. A. R., & et al. 2010, *ApJ*, 718, 632
- Hallman, E. J., O'Shea, B. W., Smith, B. D., Burns, J. O., & Norman, M. L. 2009, *ApJ*, 698, 1795
- Holder, G. P. 2002, *ApJ*, 580, 36
- Kay, S. T., Thomas, P. A., Jenkins, A., & Pearce, F. R. 2004, *MNRAS*, 355, 1091
- Kim, W. 2007, *ApJ*, 667, L5
- Komatsu, E. & Kitayama, T. 1999, *ApJ*, 526, L1
- Komatsu, E. & Seljak, U. 2002, *MNRAS*, 336, 1256
- Komatsu, E., Smith, K. M., Dunkley, J., Bennett, C. L., Gold, B., Hinshaw, G., Jarosik, N., Larson, D., Nolta, M. R., Page, L., Spergel, D. N., Halpern, M., Hill, R. S., Kogut, A., Limon, M., Meyer, S. S., Odegard, N., Tucker, G. S., Weiland, J. L., Wollack, E., & Wright, E. L. 2010, ArXiv e-prints
- Kosowsky, A. 2003, *New Astronomy Review*, 47, 939
- Kravtsov, A. V., Klypin, A., & Hoffman, Y. 2002, *ApJ*, 571, 563
- Lau, E. T., Kravtsov, A. V., & Nagai, D. 2009, *ApJ*, 705, 1129
- Lin, W. P., Jing, Y. P., Mao, S., Gao, L., & McCarthy, I. G. 2006, *ApJ*, 651, 636
- Lin, Y., Mohr, J. J., & Stanford, S. A. 2003, *ApJ*, 591, 749
- Lokas, E. L. & Mamon, G. A. 2001, *MNRAS*, 321, 155
- Lueker, M., Reichardt, C. L., Schaffer, K. K., Zahn, O., Ade, P. A. R., & et al. 2010, *ApJ*, 719, 1045
- Mantz, A., Allen, S. W., Rapetti, D., & Ebeling, H. 2010, *MNRAS*, 406, 1759
- McCarthy, I. G., Bower, R. G., Balogh, M. L., Voit, G. M., Pearce, F. R., Theuns, T., Babul, A., Lacey, C. G., & Frenk, C. S. 2007, *MNRAS*, 376, 497
- Meneghetti, M., Rasia, E., Merten, J., Bellagamba, F., Ettori, S., Mazzotta, P., Dolag, K., & Marri, S. 2010, *A&A*, 514, A93+
- Molnar, S. M., Hearn, N., Haiman, Z., Bryan, G., Evrard, A. E., & Lake, G. 2009, *ApJ*, 696, 1640
- Nagai, D., Kravtsov, A. V., & Vikhlinin, A. 2007a, *ApJ*, 668, 1
- Nagai, D., Vikhlinin, A., & Kravtsov, A. V. 2007b, *ApJ*, 655, 98
- Nagamine, K., Ostriker, J. P., Fukugita, M., & Cen, R. 2006, *ApJ*, 653, 881
- Navarro, J. F., Frenk, C. S., & White, S. D. M. 1996, *ApJ*, 462, 563
- . 1997, *ApJ*, 490, 493
- Ostriker, J. P., Bode, P., & Babul, A. 2005, *ApJ*, 634, 964
- Pearce, F. R., Thomas, P. A., & Couchman, H. M. P. 1994, *MNRAS*, 268, 953
- Pfrommer, C., Enßlin, T. A., Springel, V., Jubelgas, M., & Dolag, K. 2007, *MNRAS*, 378, 385
- Piffaretti, R. & Valdarnini, R. 2008, *A&A*, 491, 71
- Pratt, G. W., Croston, J. H., Arnaud, M., & Böhringer, H. 2009, *A&A*, 498, 361
- Rasia, E., Tormen, G., & Moscardini, L. 2004, *MNRAS*, 351, 237
- Reichardt, C. L., Ade, P. A. R., Bock, J. J., Bond, J. R., Brevik, J. A., Contaldi, C. R., Daub, M. D., Dempsey, J. T., Goldstein, J. H., Holzapfel, W. L., Kuo, C. L., Lange, A. E., Lueker, M., Newcomb, M., Peterson, J. B., Ruhl, J., Runyan, M. C., & Staniszewski, Z. 2009a, *ApJ*, 694, 1200
- Reichardt, C. L., Zahn, O., Ade, P. A. R., & et al. 2009b, *ApJ*, 701, 1958
- Rozo, E., Wechsler, R. H., Rykoff, E. S., Annis, J. T., Becker, M. R., Evrard, A. E., Frieman, J. A., Hansen, S. M., Hao, J., Johnston, D. E., Koester, B. P., McKay, T. A., Sheldon, E. S., & Weinberg, D. H. 2010, *ApJ*, 708, 645
- Ruhl, J., Ade, P. A. R., Carlstrom, J. E., & et al. 2004, in *Society of Photo-Optical Instrumentation Engineers (SPIE) Conference Series*, Vol. 5498, Society of Photo-Optical Instrumentation Engineers (SPIE) Conference Series, ed. C. M. Bradford, P. A. R. Ade, J. E. Aguirre, J. J. Bock, M. Dragovan, L. Duband, L. Earle, J. Glenn, H. Matsuhara, B. J. Naylor, H. T. Nguyen, M. Yun, & J. Zmuidzinas, 11–29
- Sarazin, C. L. 1986, *Reviews of Modern Physics*, 58, 1
- Scoville, N., Aussel, H., Brusa, M., Capak, P., Carollo, C. M., Elvis, M., Gialvalisco, M., Guzzo, L., Hasinger, G., Impey, C., Kneib, J., LeFevre, O., Lilly, S. J., Mobasher, B., Renzini, A., Rich, R. M., Sanders, D. B., Schinnerer, E., Schminovich, D., Shopbell, P., Taniguchi, Y., & Tyson, N. D. 2007, *ApJS*, 172, 1
- Sehgal, N., Bode, P., Das, S., Hernandez-Monteagudo, C., Huffenberger, K., Lin, Y., Ostriker, J. P., & Trac, H. 2010, *ApJ*, 709, 920
- Sharp, M. K., Marrone, D. P., Carlstrom, J. E., Culverhouse, T., Greer, C., Hawkins, D., Hennessy, R., Joy, M., Lamb, J. W., Leitch, E. M., Loh, M., Miller, A., Mroczkowski, T., Muchovej, S., Pryke, C., & Woody, D. 2010, *ApJ*, 713, 82
- Shaw, L. D., Zahn, O., Holder, G. P., & Doré, O. 2009, *ApJ*, 702, 368
- Sievers, J. L., Mason, B. S., Weintraub, L., Achermann, C., Altamirano, P., Bond, J. R., Bronfman, L., Bustos, R., Contaldi, C., Dickinson, C., Jones, M. E., May, J., Myers, S. T., Oyarce, N., Padin, S., Pearson, T. J., Pospieszalski, M., Readhead, A. C. S., Reeves, R., Shepherd, M. C., Taylor, A. C., & Torres, S. 2009, ArXiv e-prints
- Sijacki, D., Pfrommer, C., Springel, V., & Enßlin, T. A. 2008, *MNRAS*, 387, 1403
- Sijacki, D., Springel, V., Di Matteo, T., & Hernquist, L. 2007, *MNRAS*, 380, 877
- Stanek, R., Rasia, E., Evrard, A. E., Pearce, F., & Gazzola, L. 2010, *ApJ*, 715, 1508
- Stanek, R., Rudd, D., & Evrard, A. E. 2009, *MNRAS*, 394, L11
- Sun, M., Voit, G. M., Donahue, M., Jones, C., Forman, W., & Vikhlinin, A. 2009, *ApJ*, 693, 1142
- Teyssier, R., Moore, B., Martizzi, D., Dubois, Y., & Mayer, L. 2010, ArXiv e-prints

- Tinker, J., Kravtsov, A. V., Klypin, A., Abazajian, K., Warren, M., Yepes, G., Gottlöber, S., & Holz, D. E. 2008, *ApJ*, 688, 709
- Trac, H., Bode, P., & Ostriker, J. P. 2010, *ArXiv e-prints*
- Vanderlinde, K., Crawford, T. M., de Haan, T., Dudley, J. P., Shaw, L., & et al. 2010, *ApJ*, 722, 1180
- Vazza, F., Brunetti, G., Kritsuk, A., Wagner, R., Gheller, C., & Norman, M. 2009, *A&A*, 504, 33
- Viero, M. P., Ade, P. A. R., Bock, J. J., Chapin, E. L., & et al. 2009, *ApJ*, 707, 1766
- Vikhlinin, A., Kravtsov, A., Forman, W., Jones, C., Markevitch, M., Murray, S. S., & Van Speybroeck, L. 2006, *ApJ*, 640, 691
- Vikhlinin, A., Kravtsov, A. V., Burenin, R. A., Ebeling, H., Forman, W. R., Hornstrup, A., Jones, C., Murray, S. S., Nagai, D., Quintana, H., & Voevodkin, A. 2009, *ApJ*, 692, 1060
- White, M., Hernquist, L., & Springel, V. 2002, *ApJ*, 579, 16